Inorganic Chemistry

ARTICLE

pubs.acs.org/IC

Electronic Structure of a Low-Spin Heme/Cu Peroxide Complex: Spin-State and Spin-Topology Contributions to Reactivity

Matthew T. Kieber-Emmons,[†] Yuqi Li,[‡] Zakaria Halime,[‡] Kenneth D. Karlin,[‡] and Edward I. Solomon*[,†]

[†]Department of Chemistry, Stanford University, Stanford, California 94305, United States

[‡]Department of Chemistry, The Johns Hopkins University, Baltimore, Maryland 21218, United States

Supporting Information

ABSTRACT: This study details the electronic structure of the heme−peroxo−copper adduct $\{[(F_8)Fe(DCHIm)]\text{-}O_2\text{-}[Cu(AN)]\}^+$ ($\mathbf{LS^{AN}}$) in which O_2^{2-} bridges the metals in a μ-1,2 or "end-on" configuration. $\mathbf{LS^{AN}}$ is generated by addition of coordinating base to the parent complex $\{[(F_8)Fe]\text{-}O_2\text{-}[Cu(AN)]\}^+$ ($\mathbf{HS^{AN}}$) in which the O_2^{2-} bridges the metals in an $\mu\text{-}\eta^2\text{:}\eta^2$ or "side-on" mode. In addition to the structural change of the O_2^{2-} bridging geometry, coordination of the base changes the spin state of the heme fragment (from $S = 5/2$ in $\mathbf{HS^{AN}}$ to $S = 1/2$ in $\mathbf{LS^{AN}}$) that results in an antiferromagnetically coupled diamagnetic ground state in $\mathbf{LS^{AN}}$. The strong ligand field of the porphyrin modulates the high-spin to low-spin effect on Fe−peroxo bonding relative to nonheme complexes, which is important in the O−O bond cleavage process. On the basis of DFT calculations, the ground state of $\mathbf{LS^{AN}}$ is dependent on the Fe−O−O−Cu dihedral angle, wherein acute angles (<∼150°) yield an antiferromagnetically coupled electronic structure while more obtuse angles yield a ferromagnetic ground state. $\mathbf{LS^{AN}}$ is diamagnetic and thus has an antiferromagnetically coupled ground state with a calculated Fe−O−O−Cu dihedral angle of 137°. The nature of the bonding in $\mathbf{LS^{AN}}$ and the frontier molecular orbitals which lead to this magneto-structural correlation provide insight into possible spin topology contributions to O−O bond cleavage by cytochrome *c* oxidase.

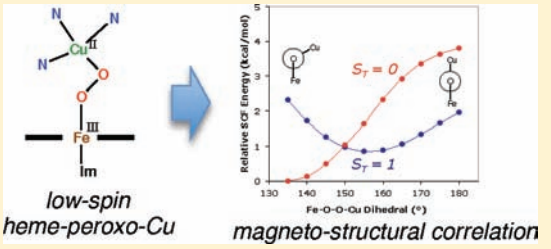

1. INTRODUCTION

Cytochrome *c* oxidase (CcO) catalyzes the terminal enzymatic step of the electron transport chain, reduction of dioxygen to water.[1,2] The source of the electrons is cytochrome *c* (cyt c), and the reaction is overall highly thermodynamically favorable. The excess free energy produced from the redox reaction is efficiently converted into a chemiosmotic potential by pumping protons from the mitochondrial matrix across the inner membrane into the intermembraneous space as follows:

$$4[(\text{cytc})]Fe^{2+} + 8H^+_{in} + O_2 \rightarrow 4[(\text{cytc})Fe]^{3+} + 2H_2O + 4H^+_{out}$$

The proton gradient is used downstream by ATP synthase to generate ATP. Despite the fact that the overall reaction is thermodynamically favorable, the first, one-electron reduction of dioxygen is uphill, necessitating sophistication at the oxygen reaction site to overcome this facet of catalysis. Nature has selected a unique heterobimetallic active site, which features a copper ion strategically juxtaposed ∼5 Å above a heme cofactor.[3,4] The copper is ligated by three histidine residues, one of which is covalently tethered to a nearby tyrosine residue, a cross-link that is thought to be functional.[5]

A simplified consensus mechanism for CcO is illustrated in Figure 1. Entry into catalysis begins from the reduced enzyme **R** with the binding of dioxygen to form intermediate **A**, which has been assigned as a formally ferric−superoxo species based on transient resonance Raman experiments.[6,7] The next intermediate, $\mathbf{P_M}$, has been assigned as a ferryl−heme−cupric hydroxide−tyrosine radical based on a variety of spectral and chemical evidence. The existence of a high-valent Fe(IV)=O in $\mathbf{P_M}$ is based on mixed O_2 isotope resonance Raman spectral studies which unequivocally demonstrated that in $\mathbf{P_M}$ the O−O bond is broken.[8] Evidence for the involvement of the cross-linked tyrosine, specifically as a net $H^\bullet$ donor, comes from ATR-FTIR,[10−12] EPR,[13] and an iodination reaction followed by degradative mass spectrometry (MS).[14]

Conversion of state **A** to $\mathbf{P_M}$ is of significant interest from a fundamental standpoint as it contains the reductive cleavage of the O−O bond. Moreover, the proposed net $H^\bullet$ abstraction from tyrosine provides impetus for study of the nature of the active oxidant. Collman and co-workers recently synthesized a binucleating scaffold derived from the picket-fence porphyrin motif wherein a copper binding site was engineered into the pocket above the heme. This system was able to abstract $H^\bullet$ from phenols both inter-[15] and intramolecularly[16] (when a phenol was tethered to one of the copper ligand arms) and reduce O_2 to H_2O under rate-limiting electron flux.[17] An Fe(III)−superoxo species was trapped and is proposed to function as the active oxidant. We and others hypothesized involvement of an unobserved peroxo intermediate during the **A** to $\mathbf{P_M}$ conversion.[18−20] A synthetic

Received: August 26, 2011
Published: October 18, 2011

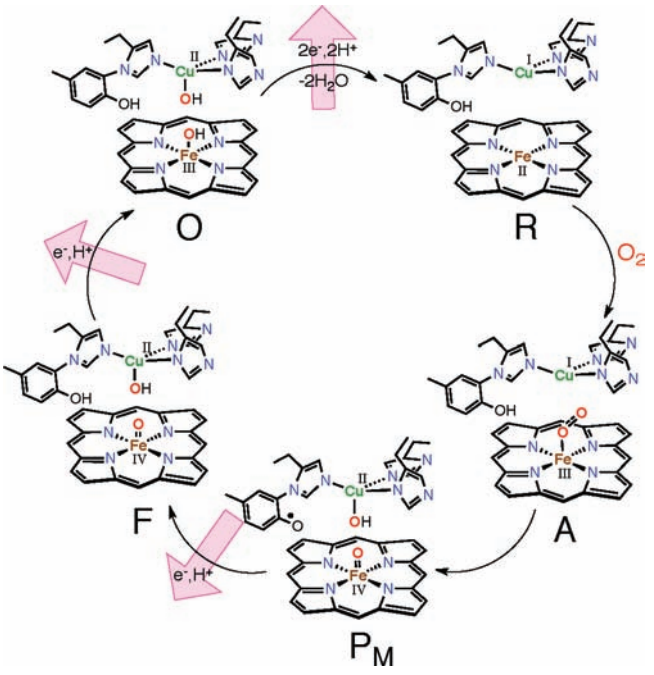

Figure 1. Schematic of the catalytic cycle of oxygen reduction by CcO. Pink arrows indicate proton-pumping steps. The axial base on heme has been omitted for clarity.

example that demonstrates the structural feasibility of such an intermediate comes from Naruta and co-workers, who succeeded in crystallographic characterization of a heme−peroxo−copper adduct that has a μ-η^2:η^1 peroxo core.[21] The synthetic strategies employed independently by Collman and Naruta involve a porphyrin ligand scaffold with a preorganized copper binding site in close proximity to the heme.[22,23] An alternative strategy using discrete heme and copper monomer components has also been successful as a result of favorable reaction kinetics.[24] In an early example,[25] reaction of a mixture of $[(F_8)Fe^{II}]$ and $[(TMPA)Cu^{I}(CH_3CN)]^+$ with dioxygen at subambient temperatures resulted in formation of $\{[(F_8)Fe]\text{-}O_2\text{-}[Cu(TMPA)]\}^+$ that, based on spectroscopic studies, also contains a μ-η^2:η^1 peroxo core.[26,27] Neither the crystallographically characterized complex nor $\{[(F_8)Fe]\text{-}O_2\text{-}[Cu(TMPA)]\}^+$ perform the biomimetic O−O bond cleavage reaction with phenols.

To test the ability of peroxo formulations for the net hydrogen atom abstraction from tyrosine, the systematic synthesis and spectroscopic definition of small molecule heme−peroxo−copper adducts with varying ligand scaffolds has been pursued. The studies have proven fruitful, including the recent preparation and spectroscopic elucidation of the heme−peroxo−copper adduct $\{[(F_8)Fe(DCHIm)]\text{-}O_2\text{-}[Cu(AN)]\}^+$ (**LS**^{AN}, AN = bis-[3-(dimethylamino)propyl]amine]) in which the peroxo moiety bridges in a μ-1,2 (η^1:η^1) or "end-on" geometry. The heme fragment of **LS**^{AN} is low-spin ($S = 1/2$) and antiferromagnetically coupled to Cu(II) ($S = 1/2$) to yield a diamagnetic ground state. **LS**^{AN} is generated from reaction of $\{[(F_8)Fe]\text{-}O_2\text{-}[Cu(AN)]\}^+$ (**HS**^{AN})[28,29] with coordinating base (dicyclohexyl imidazole, DCHIm) (Figure 2).[29] **HS**^{AN} contains a μ-η^2:η^2 or "side-on" peroxo structure type with a high-spin (HS, $S = 5/2$) ferric heme antiferromagnetically coupled through the peroxo to the Cu(II) ($S = 1/2$), resulting in an $S_T = 2$ ground state. On the basis of initial low-temperature studies,[29] **LS**^{AN} (but not **HS**^{AN}) is

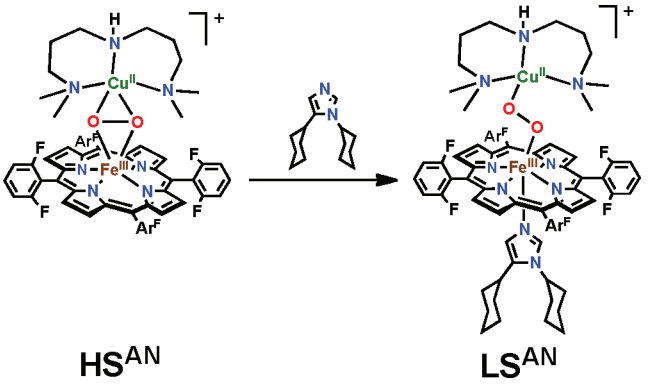

Figure 2. Addition of coordinating base to **HS**^{AN} results in formation of a distinct intermediate **LS**^{AN}.

reactive toward phenol and thus provides a unique platform to survey the factors that contribute to reactivity in heme−peroxo−copper adducts. This manuscript details the electronic structure of **LS**^{AN}, based on the correlation of spectral features with density functional theory calculations (Figure 3, using the geometry optimized truncated model from ref 30), and compares the spin-state/reactivity correlations in heme−copper adducts with that previously detailed for nonheme iron−peroxo complexes.[31] During the course of these studies, we developed a magneto-structural correlation deriving from the mechanism of magnetic superexchange in **LS**^{AN}, which has implications for spin topology contributions to O−O bond cleavage by CcO.

2. RESULTS AND ANALYSIS

2.1. Resonance Raman Excitation Profile. The absorption spectrum of **LS**^{AN} is shown in Figure 4 and is dominated by the heme spectral features at 421 (ε = 142.7 mM^{-1} cm^{-1}) and 537 nm (ε = 11.5 mM^{-1} cm^{-1}) and two low-energy features at 789 (ε = 1.5 mM^{-1} cm^{-1}) and 951 nm (ε = 0.9 mM^{-1} cm^{-1}). The resonance Raman spectrum of **LS**^{AN} displays three oxygen isotope modes at 796, 586, and 394 cm^{-1}. Previously, these bands were assigned as the ν_{O-O} (796 cm^{-1}), ν_{Fe-O} (586 cm^{-1}), and tentatively δ_{N-Fe-O} (394 cm^{-1}) modes.[30] The excitation dependence of the intensity of the ν_{O-O} and ν_{Fe-O} vibrational features (the δ_{N-Fe-O} feature was too weak to be profiled) correlate to the 789 nm absorption band in the UV−vis spectrum (Figure 4). ν_{Fe-O} is significantly more intense than ν_{O-O}, indicating the absorption band is a $O_2^{2-} \rightarrow Fe^{III}$ CT transition. Such a low-energy $O_2^{2-} \rightarrow Fe^{III}$ CT transition is unusual and is indicative of a highly covalent peroxo−iron interaction (vide infra).

2.2. Electronic Structure Calculations: Correlations to Experimental Data. To further probe the spectral features of **LS**^{AN}, DFT calculations were performed on a truncated model of **LS**^{AN} (by changing the cyclohexyl rings of the bound imidazole to methyl groups). As detailed below, the computed properties of **LS**^{AN} reproduce the experimentally observed diamagnetic ground state, the isotope-sensitive vibrational modes, the low-energy CT transitions observed optically, and the coupling of the Raman vibrational modes to the CT transition. Thus, the calculations are used to enhance the spectral assignments and to understand the peroxo−Fe and peroxo−Cu bonding in **LS**^{AN}.

2.2.1. Analytical Frequencies. The normal modes derived from an analytical frequency calculation on the optimized geometric coordinates of **LS**^{AN} were used to correlate to the

dx.doi.org/10.1021/ic2018727 |*Inorg. Chem.* 2011, 50, 11777–11786

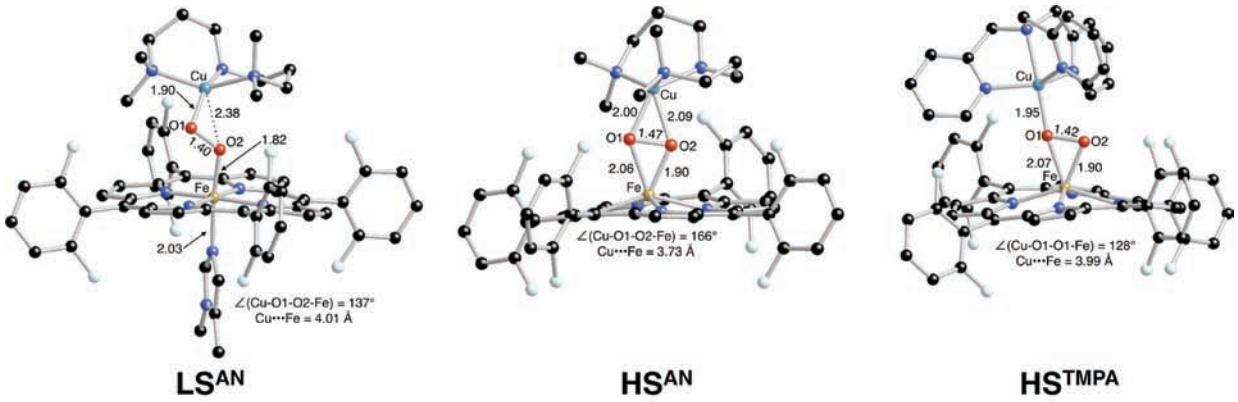

Figure 3. Optimized geometric structures of $\mathbf{LS}^{\mathbf{AN}}$, $\mathbf{HS}^{\mathbf{AN}}$, and $\mathbf{HS}^{\mathbf{TMPA}}$. Models were optimized with the BP86 functional within the spin-unrestricted formalism on the respective BS spin surfaces.

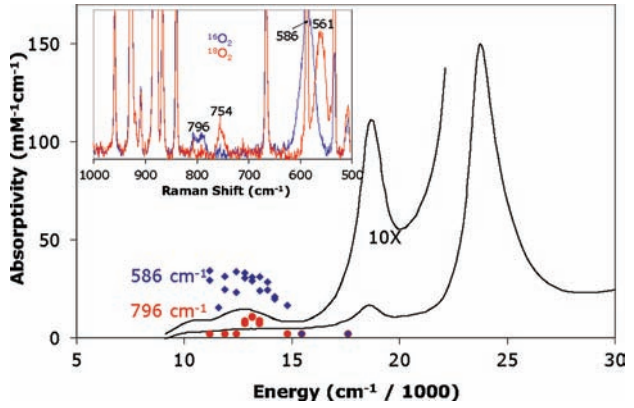

Figure 4. Resonance Raman excitation profiles of the 586 (blue diamonds) and 796 cm^{-1} (red circles) features of $\mathbf{LS}^{\mathbf{AN}}$ at 77 K in THF overlaid with the 193 K absorption spectrum (black line). (Inset) Resonance Raman spectrum of $\mathbf{LS}^{\mathbf{AN}}$ prepared with $^{16}O_2$ (blue line) and $^{18}O_2$ (red line).[30].

resonance Raman data and to verify the assignment of the isotope-sensitive bands. The potential energy distributions (PED) of the normal modes are given in Table 1. Due to the large size of the molecule, the Fe−O—O−Cu core modes coincide in energy with ligand modes and thus mix, leading to fractional components of the core modes distributed over several modes of the molecule which adds complexity to the analysis. Nonetheless, it is clear that the DFT calculation predicts oxygen isotope-sensitive clusters of modes at 840 (ν166, ν167), ~594 (ν129, ν131), and ~487 cm^{-1} (ν109, ν103) assigned as the ν_{O-O}, ν_{Fe-O}, and ν_{Cu-O} vibrations, respectively. The PED of these modes support their assignment, as indicated by the high distribution of these respective internal coordinates in the corresponding normal modes. The DFT calculations also predict a low-energy mode at 383 cm^{-1} (ν88) which downshifts to 379 cm^{-1} in the $^{18}O_2$ isotopologue. This mode, although mixed with a variety of other motion, is best described as the trans-axial $\delta_{NIm—Fe-O}$ bend, consistent with the assignment in ref 30. No other modes with significant oxygen isotope dependence were found in the calculations. ν_{Cu-O} is not observed in the resonance Raman spectrum due to a lack of Cu−O excited state distortion upon excitation into the peroxo → Fe(III) CT transition (see section 2.2.4).

2.2.2. Electronic Structure. Consistent with the observed diamagnetism in the NMR spectrum,[29] $\mathbf{LS}^{\mathbf{AN}}$ is well described as a broken-symmetry (BS) singlet ($S_T = 0$) that is calculated to be 2.2 kcal/mol lower in energy than the triplet. In this singlet, the low-spin Fe(III) and Cu(II) are antiferromagnetically coupled. The low-spin electronic configuration of the heme is a consequence of the axial ligation of imidazole. The molecular orbital diagram and key unoccupied molecular orbitals are shown in Figure 5 and Table 2. The unoccupied opposite-spin partner of a half-occupied natural orbital reflects the uncompensated spin of the occupied orbital, and thus, the unoccupied orbital can be used for analysis of the bonding. Fe(III) has a single unpaired d electron of α-spin which results in a localized unoccupied β-spin Fe $3d_{xz}$ orbital (307β). Note that for these analyses the z axis is along the Fe−O bond and the x axis is perpendicular to the O−O bond. Two additional unoccupied α/β-spin orbital pairs exist at higher energy in the Fe 3d manifold (311α, 312α, mixture of $311-313\beta$,[32] 314β) which correspond to the $3d_{x^2-y^2}$ and $3d_{z^2}$ of the LS Fe(III). The Cu(II) center has a single unpaired electron of β-spin, which results in an unoccupied α-spin Cu $3d_{x^2-y^2}$ orbital (307α). These Fe $3d_{xz}$ and Cu $3d_{x^2-y^2}$ are the magnetic orbitals and productively overlap through the peroxo π^* orbital as described below to yield an overall diamagnetic ground state. The magnitude of the coupling between the Fe and the Cu centers is calculated from the splitting between the $S_T = 0$ and 1 states using eq 1.[33] Expressed in terms of the Heisenberg−Dirac−van Vleck Hamiltonian, $-2JS_1 \cdot S_2$, the magnitude of the antiferromagnetic exchange parameter was calculated to be $J = -611$ cm^{-1}.

$$-2J = {}^{3}E - \frac{2^{BS}E - \langle S^2\rangle_{BS}\,{}^{3}E}{2 - \langle S^2\rangle_{BS}} \qquad (1)$$

The magnitude of the antiferromagnetic exchange coupling constant in $\mathbf{HS}^{\mathbf{AN}}$ between the high-spin Fe(III) and Cu(II) centers, calculated from the splitting between the $S_T = 2$ and 3 states ($-6J$), was previously determined to be $J = -759$ cm^{-1}.[29] In order to quantitatively compare the exchange interaction between $\mathbf{LS}^{\mathbf{AN}}$ and $\mathbf{HS}^{\mathbf{AN}}$, J must be expressed in terms of a sum of the individual magnetic orbital pathway contributions (eq 2) where n_A and n_B are the total number of unpaired electrons on the two metal centers, A and B, distributed over their respective 3d orbitals (i and j).[34] As reported previously for $\mathbf{HS}^{\mathbf{AN}}$,[29] a single *efficient* (out of five possible) superexchange pathway exists between

dx.doi.org/10.1021/ic2018727 |*Inorg. Chem.* 2011, 50, 11777–11786

Table 1. DFT-Derived Vibrational Modes and Potential Energy Distribution

		energy (cm^{-1})		potential energy distribution (%)					
mode	k	$^{16}O_2$	$^{18}O_2$	ν_{O-O}	ν_{Fe-O}	ν_{Cu-O}	δ_{Fe-O-O}	δ_{Cu-O-O}	δ_{N-Fe-O}
υ88	0.80	383	379	0	6	7	6	0	8
υ103	0.43	460	452	0	−2	18	−1	0	0
υ109	0.75	487	477	−1	−8	35	0	0	0
υ129	1.84	589	562	0	26	4	−11	−2	−1
υ131	1.79	594		0	20	3	−10	−1	−2
υ166	4.07	839	795	37	−2	0	0	0	0
υ167	4.17	840		36	−2	0	0	0	0

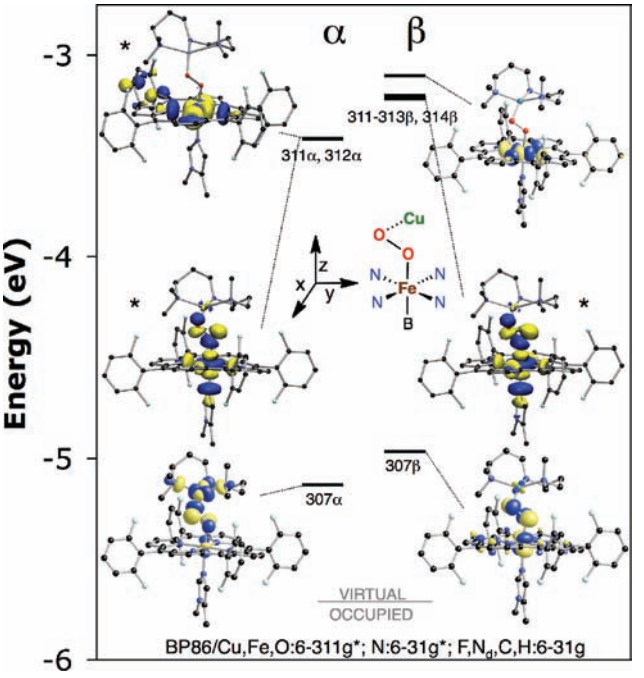

Figure 5. Molecular orbital diagram of $\mathbf{LS}^{AN}$ showing key unoccupied antibonding orbitals from a spin-unrestricted BP86 calculation (isovalue 0.05 au). Isosurface for asterisked orbitals are linear combination of orbitals (top left, $311\alpha - 312\alpha$; middle left, $311 + 312\alpha$; middle right, $311\beta - 312\beta + 313\beta$).

the five 3d orbitals on the Fe(III) and the single 3d orbital on the Cu(II) (the Fe $3d_{xz}$ and the Cu $3d_{x^2-y^2}$ orbitals interact), and its contribution to the total J value is scaled by a factor of 1/5 ($n_A = 5$, $n_B = 1$, in eq 2). A single pathway exists in $\mathbf{LS}^{AN}$ between the Cu $3d_{x^2-y^2}$ and the Fe $3d_{xz}$, and based on eq 2 with $n_A = n_B = 1$, it is considerably *less efficient* relative to $\mathbf{HS}^{AN}$. The difference in efficiency is a result of the difference in core geometries between $\mathbf{LS}^{AN}$ and $\mathbf{HS}^{AN}$. In $\mathbf{HS}^{AN}$, the side-on μ-η^2:η^2 peroxo core geometry allows for much better overlap between the respective Fe/Cu magnetic orbitals compared to the end-on μ-1,2 geometry for $\mathbf{LS}^{AN}$, the specific basis of which is explored below.

$$J = \frac{1}{n_A n_B} \sum_{i,j=1}^{n_A n_B} J_{A_i B_j} \qquad (2)$$

2.2.3. Excited States. The absorption spectrum of $\mathbf{LS}^{AN}$ (Figure 4) is dominated by the heme spectral features. Nonetheless, a relatively weak band is observed at 789 nm which is

Table 2. Mulliken Population Analysis of Unoccupied Metal- or Peroxo-Based Molecular Orbitals from a Spin-Unrestricted BP86 Calculation of $\mathbf{LS}^{AN}$ in the BS ($S_T = 0$) State

orbital	level	occ	E(eV)	Fe	O_2	Cu	rest
307α	Cu $x^2-y^2 - O_2$	0	−5.131	6.1	29.3	42.7	21.8
311α	Fe $z^2 - O_2$	0	−3.418	59.4	11.6	0.7	28.3
312α	Fe x^2-y^2	0	−3.414	60.7	6.7	0.4	28.3
307β	Fe $xz - O_2\ \pi^*_v$	0	−4.965	39.8	32.3	2.4	25.5
311β	Fe $z^2 - O_2\ \pi^*_\sigma$ + L	0	−3.217	14.6	3.8	0.1	81.5
312β	Fe $z^2 - O_2\ \pi^*_\sigma$ + L	0	−3.203	31.1	8.0	0.2	60.7
313β	Fe $z^2 - O_2\ \pi^*_\sigma$ + L	0	−3.198	18.4	4.7	0.1	76.8
314β	Fe x^2-y^2	0	−3.102	65.1	0.0	0.0	34.9
spin density				0.63	0.12, −0.10	−0.41	

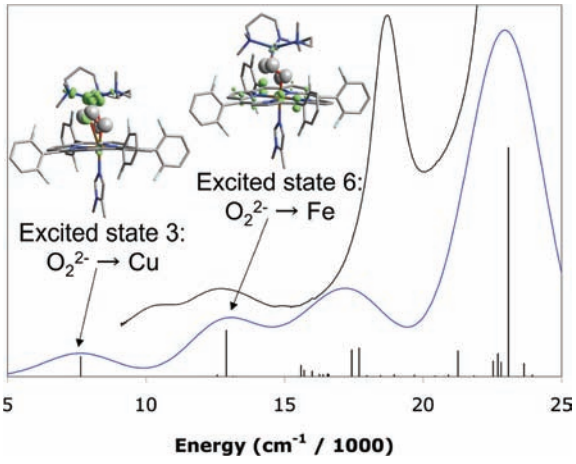

Figure 6. TD-DFT-derived absorption spectrum (blue line) generated by the individual transitions (sticks) using 3000 cm^{-1} half-width Gaussian functions. Overlaid is the experimental absorption spectrum (black line). Electron density difference maps (green, positive (gain) phase; gray, negative (loss) phase; isovalue 0.005 au) of the two low-energy LMCT transitions (excited states 3 and 6).

profiled by the ν_{Fe-O} and ν_{O-O} modes in the resonance Raman spectrum and thus assigned as a peroxo → Fe CT. To obtain quantitative insight into the origin of this feature, time-dependent (TD)-DFT calculations were performed on $\mathbf{LS}^{AN}$ within the unrestricted formalism using the B3LYP functional on the BP86-optimized model. The B3LYP functional was selected based on the best correlation to the data.[35] An absorption

dx.doi.org/10.1021/ic2018727 |*Inorg. Chem.* 2011, 50, 11777–11786

Table 3. Mulliken Population Analysis of Important Donor and Acceptor Molecular Orbitals from a TD-DFT Calculation of LS^{AN} in the BS ($S = 0$) State Using the B3LYP Functional within the Spin-Unrestricted Formalism

orbital	level	occ	E(eV)	Fe	O_2	Cu	rest
302α	Fe yz + O_2 π^*_σ	1	−7.807	14.8	18.0	4.9	62.3
303α	O_2 π^*_σ + Fe yz	1	−7.584	25.3	39.6	9.8	25.4
306α	O_2 π^*_v	1	−6.783	6.0	79.1	7.6	7.3
309α	Cu x^2-y^2 − O_2 π^*_v	0	−3.974	4.2	23.8	48.9	23.0
317α	Fe z^2 − O_2 π^*_σ	0	−2.187	62.8	16.1	1.5	19.6
302β	Fe xz + O_2 π^*_σ	1	−7.427	45.9	10.5	5.3	38.3
303β	O_2 π^*_σ + Fe yz	1	−7.207	18.5	47.2	11.9	22.5
306β	O_2 π^*_v − Fe xz	1	−6.785	13.7	67.4	3.3	15.6
307β	Por	0	−4.265	8.7	9.8	0.3	81.3
309β	Fe xz − O_2 π^*_v	0	−3.306	62.6	12.6	0.2	24.6
319β	Fe z^2 − O_2 π^*_σ	0	−1.815	68.8	13.5	0.2	17.5
spin density				0.83	0.10, −0.19	0.52	

spectrum was simulated by assuming that each transition gives rise to a Gaussian band shape with a full-width at half-maximum of 3000 cm^{-1} (Figure 6).

TD-DFT predicts two low-energy transitions at 7637 (1309 nm) and 12 894 cm^{-1} (776 nm) along with several transitions at higher energy (Table S2, Supporting Information). As is evident from inspection of the electron density difference maps (EDDMs) in Figure 6 and analysis of the donor and acceptor orbitals, both transitions are peroxo LMCT in nature. An EDDM is calculated by evaluating the electron density difference (EDD, eq 3) over space, where Ψ_a and Ψ_d are the acceptor and donor orbital transition components evaluated at a point in space and c is the transition component coefficient, summed over all transition components i. The lowest energy transition (Table 3 and Figure 7) is the O_2^{2-} π^*_v → Cu $d_{x^2-y^2}$ excitation based on the donor (306α) and acceptor (309α) orbitals (i.e., excitation of an electron from the peroxo−Cu σ-bonding MO to its σ-antibonding counterpart). This predicted transition is correlated to a low-energy absorption feature experimentally observed at 951 nm (10 515 cm^{-1}, Figure 4) suggestive of an assignment; however, the experimental feature is too low in energy to probe via resonance Raman spectroscopy. The higher energy transition has two orbital components (306β to 307β and 306β to 309β) in which the donor (306β) is the O_2^{2-} π^*_v orbital (Table 3, Figure 7). The acceptors are formally assigned as a porphyrin and Fe $3d_{xz}$ MO, respectively, based on their populations. However, due to coincidental near degeneracy these orbitals are mixed. Specifically, the 307β MO contains 8.7% Fe, 9.8% O_2^{2-}, and 80.1% porphyrin character, and the 309β MO is composed of 62.6% Fe, 12.6% O_2^{2-}, and 23.0% porphyrin. Thus, the 12 894 cm^{-1} transition is assigned as the O_2^{2-} π^*_v→ Fe $3d_{xz}$ transition (i.e., excitation of an electron from the peroxo−Fe π-bonding MO to its π-antibonding counterpart), which compares well with the experimentally determined peroxo → Fe CT at 789 nm (12 674 cm^{-1}). This assignment is consistent with the lack of porphyrin vibrations and lack of enhancement of a ν_{Cu-O} vibration in the resonance Raman spectrum upon excitation into this absorption envelope as described below.

$$\mathrm{EDD} = \sum_{i=1}^{n} c_i^2(\Psi_{ai}(x,y,z)^2 - \Psi_{di}(x,y,z)^2) \quad (3)$$

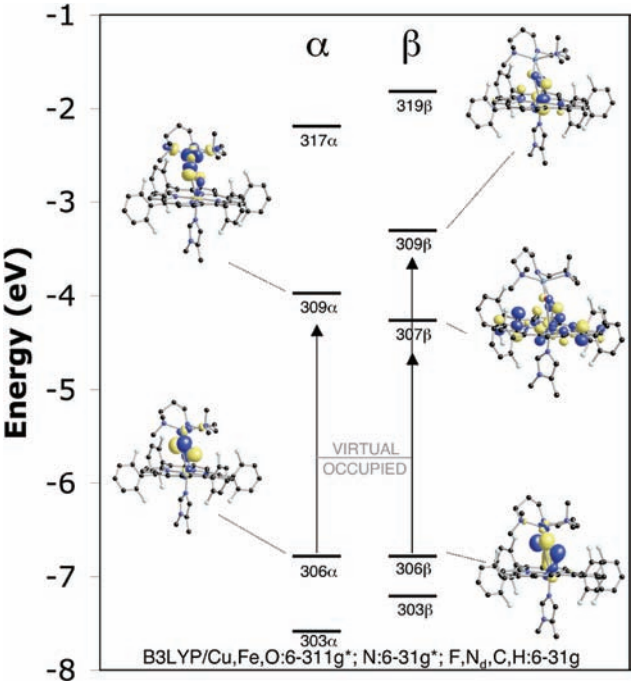

Figure 7. Molecular orbital diagram of LS^{AN} derived from a B3LYP TD-DFT calculation. Vertical arrows indicate LMCT transitions (excited states 3 and 6) which are assigned as $O_2^{2-}\pi^*_v$ → Cu $3d_{x^2-y^2}$ (left) and $O_2^{2-}\pi^*_v$ → Fe $3d_{xz}$ (right), respectively, which are the only low-energy transitions with significant intensity (see Figure 6).

2.2.4. Excited State Distortions. TD-DFT calculations were performed on LS^{AN} to predict the excited state distortions (and thus resonance enhancements in the Raman spectrum) of the normal modes ν167, ν131, ν109, and ν88 (ν_{O-O}, ν_{Fe-O}, ν_{Cu-O}, and $\delta_{NIm-Fe-O}$, respectively, see Table 4 and section 2.2.1) to evaluate the assignment of the trans-axial bend ($\delta_{NIm-Fe-O}$) at 394 cm^{-1} and to rationalize the lack of a copper−peroxo stretch (ν_{Cu-O}) upon excitation into the O_2^{2-} π^*_v → Fe $3d_{xz}$ charge transfer transition. The computational distortions were obtained by systematically varying the ground state geometry of LS^{AN} in the positive and negative directions along the respective normal mode and performing a TD-DFT calculation to determine the resulting change in the O_2^{2-} π^*_v→ Fe $3d_{xz}$ CT transition energy. The calculations provide a value for $(\Delta E^{\text{TD-DFT}}_{O_2\rightarrow Fe}/\Delta Q_k)_0$, the excited state distorting force along mode Q_k, where ΔE is the change in the excitation energy and ΔQ_k is the dimensionless nuclear distortion parameter of the kth normal mode. The value $(\Delta E^{\text{TD-DFT}}_{O_2\rightarrow Fe}/\Delta Q_k)_0$ is equivalent to a first-order electron−nuclear coupling term when the distortion from the equilibrium geometry is small.

The energy of the calculated O_2^{2-} → Fe $3d_{xz}$ CT transition (Table 4 and Figure 8) was significantly altered when the molecular geometry was stepped along the ν_{O-O}, ν_{Fe-O}, and $\delta_{NIm-Fe-O}$ modes, indicating large excited state distortions (1.139, 2.820, −1.184 erg × 10^{12}, respectively). In contrast, the CT energy perturbation by distortion along the ν_{Cu-O} mode is minimal, indicating a very small excited state distortion along this mode (0.137 erg × 10^{12}). Thus, excitation into the O_2^{2-} → Fe(III) CT transition is expected to produce little if any resonance Raman intensity for the ν_{Cu-O} mode, consistent with experiment. The excited state distortion forces were also calculated for the O_2^{2-} → Cu(II) CT transition predicted at

dx.doi.org/10.1021/ic2018727 |Inorg. Chem. 2011, 50, 11777–11786

Table 4. Summary of DFT-Derived Excited State Distortion Parameters

	ν88 ($\delta_{NIm—Fe—O}$)		ν109 ($\nu_{Cu—O}$)		ν131 ($\nu_{Fe—O}$)		ν167 ($\nu_{O—O}$)	
	$O_2 \rightarrow$ Cu	$O_2 \rightarrow$ Fe	$O_2 \rightarrow$ Cu	$O_2 \rightarrow$ Fe	$O_2 \rightarrow$ Cu	$O_2 \rightarrow$ Fe	$O_2 \rightarrow$ Cu	$O_2 \rightarrow$ Fe
$(\Delta E_{CT}^{calcd}/\Delta Q_k)_0$ (erg $\times 10^{12}$)	0.082	−1.184	−0.429	0.137	1.588	2.820	0.710	1.139
k_{calcd} (mDyn/Å)	0.797		0.749		1.789		4.17	

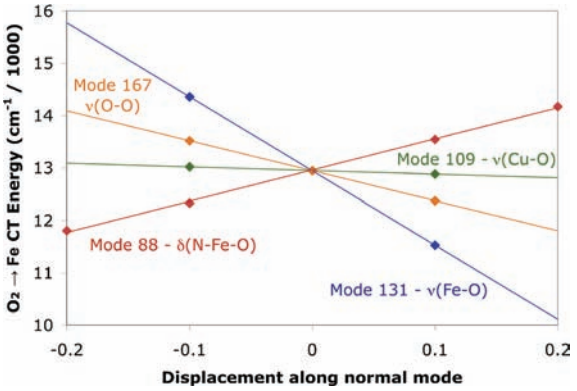

Figure 8. Dependence of the $O_2^{2-}\pi^*_\nu \rightarrow$ Fe $3d_{xz}$ CT transition energy of $\mathbf{LS}^{AN}$ on the displacement of the metrical parameters along the normal modes ν167 (orange line), ν131 (blue line), ν109 (green line), and ν88 (red line) determined by unrestricted B3LYP TD-DFT calculations with an $S = 0$ ground state.

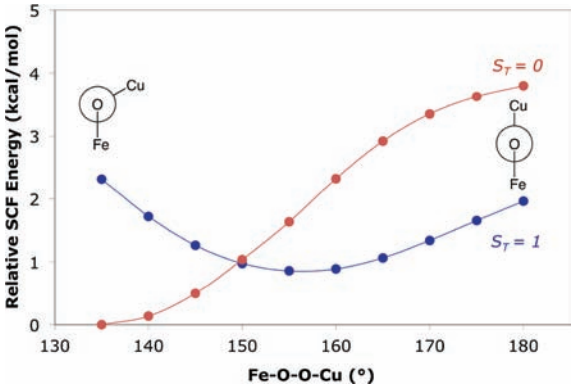

Figure 9. DFT (BP86) relaxed potential energy scan of the Fe—O—O—Cu dihedral angle of $\mathbf{LS}^{AN}$ on the triplet surface (blue line) and SP energy on the spin-purified singlet surface (red line). Newman projections are along the O—O vector.

7627 cm^{-1}. Excitation into this band would lead to enhancement of the $\nu_{Cu—O}$, $\nu_{O—O}$, and $\nu_{Fe—O}$ modes and little (if any) enhancement of the $\delta_{NIm—Fe—O}$ mode.

2.3. Electronic Structure Calculations: Nature of Bonding. *2.3.1. Fe—Peroxo Bond.* The composition and assignment of key unoccupied molecular orbitals are given in Table 2 and graphically depicted in the diagram in Figure 5 (key occupied molecular orbitals are given in Table S1, Supporting Information). Upon binding to Fe, the doubly degenerate fully occupied peroxo π^* orbitals split into π^*_σ and the π^*_ν, where the z axis is along the Fe—O vector and π^*_σ is in the Fe—O—O plane. Both π^*_σ and π^*_ν contribute to the bond with the Fe in $\mathbf{LS}^{AN}$. The dominant interaction is of σ-bonding character and consists of donation from the filled π^*_σ of the peroxo (299α and 304β) into the unoccupied Fe d_{z^2} (the unoccupied spin-up d_{z^2} mixes into $311\alpha-312\alpha$, and the unoccupied spin-down d_{z^2} mixes into $311\beta-313\beta$). The second significant interaction which is of π-bonding character is the donation of the filled π^*_ν of the peroxo (303β) into the half-occupied Fe d_{xz} orbital (307β). These interactions between O_2^{2-} and Fe(III) lead to a net very covalent bond, as quantified by the mixing of O_2^{2-} character into the unoccupied Fe d orbitals. In the spin-up σ-antibonding orbital (Fe $3d_{z^2} - O_2^{2-}\ \pi^*_\sigma$, 311α), the contributions are 59.4% Fe and 11.6% O_2^{2-}, and in the spin-down partner (mixture of $311\beta-313\beta$), 64.1% Fe and 16.5% O_2^{2-}. The π-antibonding orbital (Fe $3d_{xz} - O_2^{2-}\ \pi^*_\nu$, 307β) is composed of 32.3% O_2^{2-} and 39.8% Fe.

The Fe—peroxo interaction in $\mathbf{LS}^{AN}$ is significantly more covalent than that found for $\mathbf{HS}^{AN}$. Quantitatively, the σ and π bonding in $\mathbf{HS}^{AN}$ consists of a single peroxo donor interaction with a half-occupied Fe d orbital in which the antibonding O_2^{2-} orbital contributions are 18.5% for σ and 13.4% for π. As described above, the peroxo total σ- and π-donor contributions for $\mathbf{LS}^{AN}$ are 28.1% and 32.3%, respectively. The increase in Fe—peroxo covalency of $\mathbf{LS}^{AN}$ results from (1) the LS Fe(III) electronic structure that leads to a lack of repulsion in the σ-bonding framework because Fe $3d_{z^2}$ is unoccupied and (2) a strong π-donor bonding interaction between the peroxo π^* orbital and Fe due to the shorter Fe—O distance ($\mathbf{LS}^{AN}$ = 1.82 Å; $\mathbf{HS}^{AN}$ = 2.06, 1.90 Å). The increased Fe—peroxo covalency of $\mathbf{LS}^{AN}$ significantly impacts the O—O bond relative to $\mathbf{HS}^{AN}$ due to the nature of the peroxo donor orbitals that are π antibonding with respect to the O—O bond. A stronger Fe—O bond would be expected to strengthen the O—O bond. A strengthening of the O—O bond in $\mathbf{LS}^{AN}$ is reflected in the shorter O—O bond distance (1.40 Å) compared to that of $\mathbf{HS}^{AN}$ (1.47 Å). However, this correlation is complicated by differences in Cu bonding (side-on versus end-on) which dominates the O—O bond strength for $\mathbf{HS}^{AN}$ and is considered further below.

2.3.2. Cu—Peroxo Bond. The composition and assignments of key unoccupied molecular orbitals are given in Table 2 and are graphically depicted in the diagram in Figure 5 (key occupied molecular orbitals are given in Table S1, Supporting Information). The Cu—peroxo bonding in $\mathbf{LS}^{AN}$ is dominated by a single interaction of σ character. This interaction consists of donation from the filled $O_2^{2-}\ \pi^*$ into the singly occupied Cu $3d_{x^2-y^2}$ orbital (307α). The interaction is also very covalent, with 29.3% of O_2^{2-} character mixed into the spin-up Cu-based hole (307α). The $O_2^{2-}\ \pi^*$ contribution is a mixture of π^*_σ and π^*_ν orbital components (19.7% and 9.4%, respectively)[36] as a result of maximizing overlap between the $O_2^{2-}\ \pi^*$ and the Cu 3d hole, which is dictated by the Fe—O—O—Cu dihedral angle competing against the sterics of the ligand scaffold (see below).

The magnitude of the Cu—peroxo donor interactions in $\mathbf{LS}^{AN}$ and $\mathbf{HS}^{AN}$ are similar. In $\mathbf{HS}^{AN}$, in which $O_2^{2-}\ \pi^*_\sigma$ interacts with Cu $3d_{x^2-y^2}$, the Cu-based hole is composed of 41.4% Cu and

dx.doi.org/10.1021/ic2018727 |Inorg. Chem. 2011, 50, 11777–11786

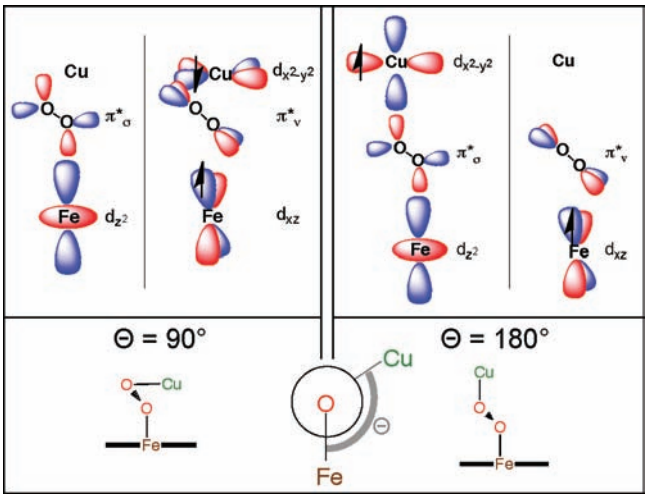

Figure 10. Orbital basis for the dependence of the ground state spin of $\mathbf{LS}^{\mathbf{AN}}$ on the Fe−O—O−Cu dihedral angle Θ in the limits of 90° (left) and 180° (right). Dihedral angle governs the interaction of the Cu hole with the two peroxo π^* orbitals.

29.6% O_2 character.[29] Thus, despite the fact that in $\mathbf{HS}^{\mathbf{AN}}$ the peroxo is bound η^2 rather than η^1 as in $\mathbf{LS}^{\mathbf{AN}}$, the Cu−peroxo covalencies are equivalent. While the σ-donor covalencies are similar in magnitude, the side-on geometry of $\mathbf{HS}^{\mathbf{AN}}$ allows for a backbonding interaction between Cu and O_2^{2-}, in which a filled Cu d orbital contributes electron density into the antibonding O_2^{2-} σ^* orbital (see ref29 for details). This backbonding is not present in $\mathbf{LS}^{\mathbf{AN}}$ due to the η^1 peroxo coordination to the Cu.

2.3.3. Dependence of the Ground State on Fe−O−O−Cu Dihedral Angle. A relaxed potential energy scan was performed on $\mathbf{LS}^{\mathbf{AN}}$ with the BP86 functional to assess the behavior of the singlet and triplet PES along the Fe−O−O−Cu coordinate. Calculations using the B3LYP functional and performed in an analogous manner qualitatively reproduce the results of the BP86 calculations. The Fe−O−O−Cu dihedral angle of $\mathbf{LS}^{\mathbf{AN}}$ was distorted in 5° increments from 135° to 180°, and the remaining geometric parameters were allowed to relax on the triplet surface. Single-point energies on the BS ($S_T = 0$) surface were performed at each point and spin projected (Figure 9) to allow comparison between the energies of the singlet and triplet surfaces. At Fe−O−O−Cu dihedral angles less than ∼150°, the calculations predict the singlet to be lower in energy. In contrast, at dihedral angles above ∼150°, the triplet state is predicted to be lowest in energy. Consequently, DFT calculations predict minima on the triplet and BS surface which vary in the Fe−O−O−Cu dihedral angle with minimum energy values at ∼155° and ∼140°, respectively.

An angular overlap model can be used to describe the spin state dependence on the Fe−O−O−Cu dihedral angle. In the planar Fe−O−O−Cu dihedral limit (180°, Figure 10, right), O_2^{2-} π^*_σ interacts with the singly occupied Cu $d_{x^2-y^2}$ and the unoccupied Fe $3d_{z^2}$ orbitals and the orthogonal O_2^{2-} π^*_v orbital interacts with Fe $3d_{xz}$. In this case, the magnetic orbitals (Fe $3d_{xz}$ and Cu $3d_{x^2-y^2}$) are orthogonal, resulting in a ferromagnetically coupled electronic configuration. As the Fe−O−O−Cu dihedral angle distorts away from planar, the Cu $3d_{x^2-y^2}$ overlap with the O_2^{2-} π^*_σ decreases and overlap with the O_2^{2-} π^*_v increases. In the 90° limit (not accessible in $\mathbf{LS}^{\mathbf{AN}}$ due to sterics) Cu $3d_{x^2-y^2}$ would interact exclusively with O_2^{2-} π^*_v (Figure 10 left). The O_2^{2-} π^*_v also interacts with the singly occupied Fe $3d_{xz}$ orbital, and thus, there is overlap of the magnetic orbitals that results in an antiferromagnetically coupled ground state for dihedral angles < ∼150°. Note that the low efficiency of superexchange in $\mathbf{LS}^{\mathbf{AN}}$ compared to $\mathbf{HS}^{\mathbf{AN}}$ as quantified by a smaller J reflects the decreased overlap with the peroxo π^*_v as a result of the Fe−O—O−Cu dihedral angle of 137°, as the peroxo π^*_v is the *only* pathway in $\mathbf{LS}^{\mathbf{AN}}$ that can allow for superexchange between the half-occupied Fe and Cu orbitals. In contrast, the Fe−O—O−Cu dihedral has minimal impact on the superexchange in $\mathbf{HS}^{\mathbf{AN}}$ because both π^*_σ and π^*_v overlap with magnetic orbitals on the Fe and thus are effective pathways.

3. DISCUSSION

Impact of Heme Spin State on the O−O Bond and Correlation to Non-Heme Iron. To assess the impact of the spin state of the heme on the peroxo moiety in heme−peroxo−copper complexes, three species were compared ($\mathbf{LS}^{\mathbf{AN}}$, $\mathbf{HS}^{\mathbf{AN}}$, and $\{[(F_8)Fe]\text{-}O_2\text{-}[Cu(TMPA)]\}^+$ ($\mathbf{HS}^{\mathbf{TMPA}}$)). These three complexes are spectroscopically well characterized, and DFT structures are available wherein the peroxo group bridges the metals in a μ-1,2, μ-η^2:η^2, and μ-η^2:η^1 fashion, respectively (Figure 3). The DFT-calculated O−O bond lengths are used as a probe of the bonding within the peroxo group. Previously, we described the affect of η^2 coordination of peroxo to copper in $\mathbf{HS}^{\mathbf{AN}}$. In this configuration, backbonding from the Cu d manifold into O_2^{2-} σ^* significantly weakens the O−O bond and is reflected in a long (1.47 Å) O−O bond length. In both $\mathbf{HS}^{\mathbf{TMPA}}$ and $\mathbf{HS}^{\mathbf{AN}}$ the peroxo is coordinated η^2 to Fe, and the Fe−O bonds lengths are the same. However, $\mathbf{HS}^{\mathbf{TMPA}}$ has η^1 coordination to Cu and thus no backbonding, which results in a significantly shorter O−O bond length (1.43 Å) in $\mathbf{HS}^{\mathbf{TMPA}}$. $\mathbf{LS}^{\mathbf{AN}}$ has the shortest calculated O−O bond length (1.40 Å), indicating $\mathbf{LS}^{\mathbf{AN}}$ has a significantly stronger O−O bond than both $\mathbf{HS}^{\mathbf{AN}}$ and $\mathbf{HS}^{\mathbf{TMPA}}$.

To achieve a stronger O−O bond in $\mathbf{LS}^{\mathbf{AN}}$, the peroxo group must be a better donor to the Fe, which is strongly modulated by the spin of the heme. Upon binding the axial base, the Fe e_g orbitals are destabilized as the Fe is pulled into the porphyrin plane. The Fe d_{z^2} orbital is destabilized by virtue of having an additional axial donor interaction, and the Fe $d_{x^2-y^2}$ orbital is strongly destabilized by a more efficient interaction with the porphyrin, which together result in a low-spin heme ground state in $\mathbf{LS}^{\mathbf{AN}}$. The low-spin ground state of the heme yields a significantly more covalent Fe−peroxo interaction in $\mathbf{LS}^{\mathbf{AN}}$ due to the lack of electron−electron repulsion between O_2^{2-} π^*_σ and Fe d_{z^2}. This stronger Fe−O interaction leads to a stronger O−O bond, due to the nature of the peroxo donor orbital which is antibonding with respect to the O−O bond.

The correlation of a more covalent Fe−O interaction in the LS heme of $\mathbf{LS}^{\mathbf{AN}}$ leading to a *stronger* O−O bond is opposite of the behavior observed in nonheme iron, in which a more covalent Fe−O in LS adducts results in a *weaker* O−O bond.[31,37] In HS and LS nonheme iron complexes, the π-bonding contributions are of similar magnitude and the bonding differences are found in the σ-bonding framework. Specifically, in nonheme iron the valence orbitals of Fe are of appropriate energy to potentially interact with the in-plane π^* or π orbitals of the peroxo. Upon going from HS to LS in nonheme Fe, the peroxo donor contribution to the Fe−O σ-bonding shifts from π^* to π^b in character. In contrast, upon going from HS to LS in heme, where

dx.doi.org/10.1021/ic2018727 |*Inorg. Chem.* 2011, 50, 11777–11786

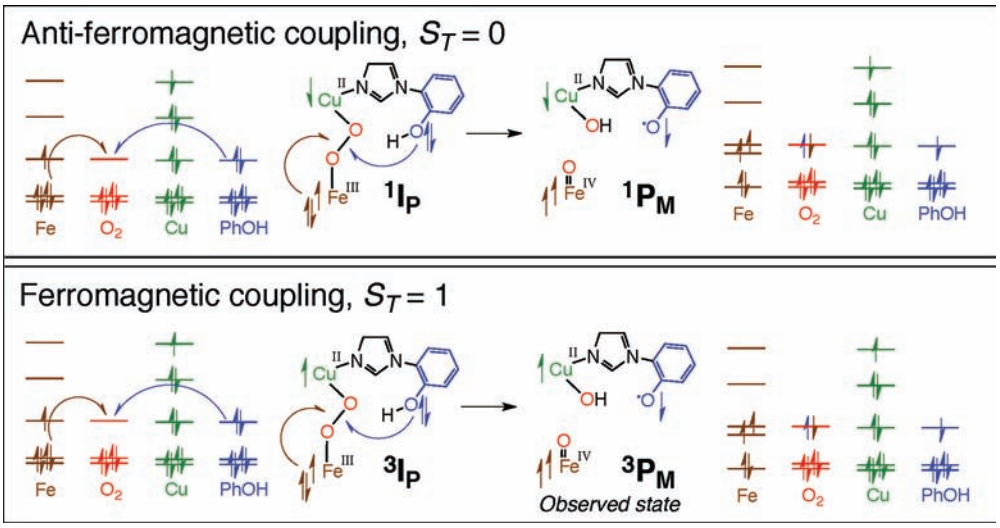

Figure 11. Illustration of the spin topology of a hypothetical enzymatic peroxo ($\mathbf{I_P}$)[19] O−O bond cleavage reaction to yield **PM** starting from an antiferromagnetic (top) or ferromagnetic (bottom) coupled ground state. Two electrons (an α,β pair) originating from Fe and Tyr244 (PhOH) fill the σ^* of the oxygen to break the O−O bond.

the ligand field of the porphyrin in the LS case strongly destabilizes the Fe e_g orbitals, a bonding interaction with the in-plane π^b of the peroxo is not available. The general result obtained here for HS to LS correlation in heme versus nonheme iron has important implications for reactivity of a putative peroxo level intermediate in CcO, namely, the putative LS peroxo−heme intermediate would have a strong O−O bond that would disfavor O−O bond homolysis. A strong O−O bond in LS peroxo−heme indicates a less reduced peroxo moiety, which would suggest a more electrophilic reactivity behavior, consistent with the possibility of net H-atom abstraction from the active site tyrosine as is proposed to generate the consensus tyrosyl radical in CcO intermediate state $\mathbf{P_M}$.

Magneto-Structural Correlation of $\mathbf{LS^{AN}}$. The singly occupied orbital on the Fe in $\mathbf{LS^{AN}}$ is of $3d_{xz}$ character (where the O−O vector defines the y axis), as a result of the π-donor interaction with the peroxo π^*_v orbital. To achieve an efficient superexchange pathway, the Fe−O−O−Cu dihedral angle is torsionally distorted to maximize the overlap between the magnetic orbitals on the metals, for which there is an energetic advantage (calculated to be 2.2 kcal/mol with BP86), consistent with the observed diamagnetism of $\mathbf{LS^{AN}}$. Specifically, since the magnetic orbital on the Fe is $3d_{xz}$ and interacts with the peroxo π^*_v, the singly occupied orbital on the Cu must also interact with the π^*_v to participate in a magnetic exchange interaction. A planar core (Figure 10, right) would result in the magnetic orbital on the Cu interacting with the peroxo π^*_σ, an orbital which donates into the unoccupied Fe $3d_{z^2}$. Under this scenario, the magnetic orbitals on the Cu and Fe would be orthogonal and thus ferromagnetically coupled. This possibility of ferromagnetic coupling can only exist when the Fe is LS, as any Fe−O−O−Cu angle in a HS heme ($S = 5/2$) would result in the overlap of magnetic orbitals, and an antiferromagnetic ground state. The fact that the 1/2 occupied Cu d orbital has 9.4% π^*_σ and only 19.7% π^*_v explains its relatively low J value. The possibility of ferromagnetic coupling for a LS Fe(III)−peroxo−Cu(II) species is potentially important for O−O bond cleavage as described below.

Effect of Magnetic Coupling on the Spin Topology of O−O Bond Rupture. We and others hypothesized the involvement of an unobserved, intermediate peroxo moiety during CcO catalysis. Due to the architecture of the CcO active site, namely, the distance between the heme a_3 and the Cu_B that has been crystallographically determined as >4.5 Å, a putative end-on bridging peroxo intermediate would be expected to adopt an Fe−O−O−Cu dihedral angle > 150° in order to span the metals. From Figure 9, this would be within the ferromagnetic regime developed for $\mathbf{LS^{AN}}$. Ferromagnetic coupling in such a putative species could impart a significant functional role, namely, the ability to cleave the O−O bond without a spin surface crossing.

Cleavage of the peroxo O−O bond requires two electrons. A μ-1,2 peroxo-bridged state could be either antiferromagnetic or ferromagnetic coupled (Figure 11, left) with $S_T = 0$ or 1, respectively, as a consequence of coupling between the LS ferric heme ($S = 1/2$) and the Cu(II) ion ($S = 1/2$). The final state, $\mathbf{P_M}$, consists of an Fe(IV)=O ($S = 1$), a Cu(II)−OH ($S = 1/2$), and a Tyr244$^\bullet$ ($S = 1/2$). The spectroscopic data of $\mathbf{P_M}$ suggests the Cu(II)−OH and Tyr244$^\bullet$ are antiferromagnetically coupled.[38] Thus, the final two electrons required to cleave the peroxo O−O bond would come from the Fe(III) (to generate the Fe(IV)=O) and the Tyr244 (to generate a Tyr244$^\bullet$ radical). These two electrons are accepted by the peroxo σ^* orbital and hence must be of opposite spin. In order to generate an $S = 1$ Fe(IV)=O, wherein the singly occupied orbitals are of $3d_{xz}$ and $3d_{yz}$ character, the electron that originates from the Fe $3d_{yz}$ and is accepted by the peroxide σ^* is *spin-down*. The second electron that comes from the Tyr, therefore, must be *spin up*. In a situation where the Cu and Fe in the putative peroxo intermediate are antiferromagnetically coupled, removal of a spin-up electron from the Tyr would result in an electronic configuration where the unpaired electrons in both the Cu^{II} and the Tyr$^\bullet$ would be spin down (Figure 11, top right) and would necessitate a spin-surface crossing to access the final antiferromagnetic state for Tyr$^\bullet$ and Cu^{II} in $\mathbf{P_M}$. In contrast, in a situation where the Cu and Fe in the putative peroxo intermediate are ferromagnetically coupled (Figure 11, bottom left), removal of a spin-up electron

dx.doi.org/10.1021/ic2018727 |*Inorg. Chem.* 2011, 50, 11777–11786

from Tyr would result in an unpaired spin-down electron on Tyr•, and thus, the final antiferromagnetically coupled Cu(II)−Tyr• state would be reached without a surface crossing. The antiferromagnetic coupling of the Tyr• with the Cu(II) reflects an efficient superexchange pathway, which in turn means overlap of the redox-active molecular orbitals. The overlap of these orbitals is a necessary condition for facile electron transfer of the fourth and final electron from the cross-linked Tyr through the copper to cleave the O−O bond. Current studies (both chemical and computational) are underway to develop further quantitative insight into the mechanism of O−O bond cleavage in $\mathbf{LS}^{\mathbf{AN}}$ and its relation to O−O bond cleavage by CcO where the Tyr is covalently tethered to the Cu-bound His ligand.

5. EXPERIMENTAL METHODS

Resonance Raman. Samples were prepared by exposure of a 1 mM solution of $[(F_8)Fe(II)]$ and $[(AN)Cu(I)]B(C_6F_5)_4$ in THF to dioxygen at subambient temperatures (−80 °C) in 5 mm rubber septa-capped NMR tubes. DCHIm (1 equiv) was added, and the tube was flame sealed. Isotopically labeled ($^{18}O_2$) samples were prepared with $^{18}O_2$ in an analogous manner. Samples were excited at a variety of wavelengths using either a Coherent I90C-K Kr+ ion laser, a Coherent 25/7 Sabre Ar+ ion laser, or an Ar+-pumped Coherent Ti:Saph laser, while the sample was immersed in a liquid nitrogen-cooled (77 K) EPR finger dewar (Wilmad). The power was ∼2 mW at the sample for the high-energy lines and >200 mW at the low-energy lines. Data were recorded while rotating the sample to minimize photodecomposition. The spectra were recorded using a Spex 1877 CP triple monochromator with 600, 1200, or 2400 grooves/mm holographic spectrograph grating and detected by an Andor Newton CCD cooled to −80 °C (for high-energy excitation) or an Andor IDus CCD cooled to −80 °C (for lowenergy excitation). Spectra were calibrated on the energy axis to toluene. Excitation profiles were intensity calibrated to the solvent (THF) by peak fitting in the program Origin.

Calculations. Density functional theory (DFT) calculations were performed using Gaussian03.[39] The optimized molecular structures of $\mathbf{LS}^{\mathbf{AN}}$, $\mathbf{HS}^{\mathbf{AN}}$, and $\mathbf{HS}^{\mathbf{TMPA}}$ have been reported previously (with cyclohexyl rings truncated to methyl groups in the case of $\mathbf{LS}^{\mathbf{AN}}$), in which the molecular structures were optimized using the BP86 functional within the spin-unrestricted formalism.[26] The basis sets employed on Fe, Cu, and O_2 were of triple-ζ-quality with polarization (6-311 g*). A double-ζ-quality, split-valence basis was used on all other atoms (6-31 g) and augmented with polarization on the metal-bound N atoms (6-31 g*). An ultrafine integration grid was employed as was auto density fitting. Due to spin effects on the Fe−O−O−Cu dihedral angle (vide supra), a one-dimensional relaxed potential energy surface (1D PES) scan was performed in 5° steps from 135° to 180° using both the BP86 and the B3LYP functionals. The scans were performed on the HS surface; then single-point energies were calculated on the BS surface. Molecular orbitals, transition densities, and simulated TD absorption spectra were visualized using Lumo.[40] Mulliken population analyses were performed using QMForge.[41] Vibrational frequency analysis was performed using VEDA4 adapted for large molecules (XL version).[42]

■ ASSOCIATED CONTENT

Supporting Information. Additional computational output. This material is available free of charge via the Internet at http://pubs.acs.org.

■ AUTHOR INFORMATION

Corresponding Author

*E-mail: edward.solomon@stanford.edu.

■ ACKNOWLEDGMENT

These studies were supported by the National Institutes of Health (NIH) (DK031450 to E.I.S.; GM60353 to K.D.K.). M.K.E. is supported by an NIH postdoctoral fellowship (GM085914). Computational resources were provided in part by the NSF through Teragrid resources provided by the NCSA (CHE080054N).

■ REFERENCES

(1) Ferguson-Miller, S.; Babcock, G. T. *Chem. Rev.* **1996**, *96*, 2889.
(2) Kaila, V. R. I.; Verkhovsky, M. I.; Wikström, M. *Chem. Rev.* **2010**, *110*, 7062.
(3) Tsukihara, T.; Aoyama, H.; Yamashita, E.; Tomizaki, T.; Yamaguchi, H.; Shinzawa-Itoh, K.; Nakashima, R.; Yaono, R.; Yoshikawa, S. *Science* **1996**, *272*, 1136.
(4) Iwata, S.; Ostermeier, C.; Ludwig, B.; Michel, H. *Nature* **1995**, *376*, 660.
(5) Das, T. K.; Pecoraro, C.; Tomson, F. L.; Gennis, R. B.; Rousseau, D. L. *Biochemistry* **1998**, *37*, 14471.
(6) Varotsis, C.; Woodruff, W. H.; Babcock, G. T. *J. Biol. Chem.* **1990**, *265*, 11131.
(7) Han, S.; Ching, Y. C.; Rousseau, D. L. *Biochemistry* **1990**, *29*, 1380.
(8) Proshlyakov, D. A.; Ogura, T.; Shinzawa-Itoh, K.; Yoshikawa, S.; Appelman, E. H.; Kitagawa, T. *J. Biol. Chem.* **1994**, *269*, 29385–29388.
(9) Proshlyakov, D. A.; Ogura, T.; Shinzawa-Itoh, K.; Yoshikawa, S.; Appelman, E. H.; Kitagawa, T. *J. Biol. Chem.* **1994**, *269*, 29385.
(10) Iwaki, M.; Breton, J.; Rich, P. R. *Biochim. Biophys. Acta* **2002**, *1555*, 116.
(11) Iwaki, M.; Puustinen, A.; Wikström, M.; Rich, P. R. *Biochemistry* **2003**, *42*, 8809.
(12) Iwaki, M.; Puustinen, A.; Wikström, M.; Rich, P. R. *Biochemistry* **2004**, *43*, 14370.
(13) Oganesyan, V. S.; White, G. F.; Field, S.; Marritt, S.; Gennis, R. B.; Yap, L. L.; Thomson, A. J. *J. Biol. Inorg. Chem.* **2010**, *15*, 1255.
(14) Proshlyakov, D. A.; Pressler, M. A.; DeMaso, C.; Leykam, J. F.; DeWitt, D. L.; Babcock, G. T. *Science* **2000**, *290*, 1588.
(15) Collman, J. P.; Decreau, R. A.; Sunderland, C. J. *Chem. Commun.* **2006**, 3894.
(16) Collman, J. P.; Decreau, R. A.; Yan, Y. L.; Yoon, J.; Solomon, E. I. *J. Am. Chem. Soc.* **2007**, *129*, 5794.
(17) Collman, J. P.; Devaraj, N. K.; Decreau, R. A.; Yang, Y.; Yan, Y. L.; Ebina, W.; Eberspacher, T. A.; Chidsey, C. E. D. *Science* **2007**, *315*, 1565.
(18) Blomberg, M. R. A.; Siegbahn, P. E. M.; Babcock, G. T.; Wikström, M. *J. Inorg. Biochem.* **2000**, *80*, 261.
(19) Blomberg, M. R. A.; Siegbahn, P. E. M.; Wikström, M. *Inorg. Chem.* **2003**, *42*, 5231.
(20) Proshlyakov, D. A.; Pressler, M. A.; Babcock, G. T. *Proc. Natl. Acad. Sci. U.S.A.* **1998**, *95*, 8020.
(21) Chishiro, T.; Shimazaki, Y.; Tani, F.; Tachi, Y.; Naruta, Y.; Karasawa, S.; Hayami, S.; Maeda, Y. *Angew. Chem., Int. Ed. Engl.* **2003**, *42*, 2788.
(22) Collman, J. P.; Boulatov, R.; Sunderland, C. J.; Fu, L. *Chem. Rev.* **2004**, *104*, 561.
(23) Kim, E.; Chufan, E. E.; Kamaraj, K.; Karlin, K. D. *Chem. Rev.* **2004**, *104*, 1077.
(24) Chufan, E. E.; Puiu, S. C.; Karlin, K. D. *Acc. Chem. Res.* **2007**, *40*, 563.
(25) Ghiladi, R. A.; Hatwell, K. R.; Karlin, K. D.; Huang, H. W.; Moënne-Loccoz, P.; Krebs, C.; Huynh, B. H.; Marzilli, L. A.; Cotter, R. J.; Kaderli, S.; Zuberbühler, A. D. *J. Am. Chem. Soc.* **2001**, *123*, 6183.

(26) del Rio, D.; Sarangi, R.; Chufan, E. E.; Karlin, K. D.; Hedman, B.; Hodgson, K. O.; Solomon, E. I. *J. Am. Chem. Soc.* **2005**, *127*, 11969.
(27) Ghiladi, R. A.; Chufan, E. E.; del Rio, D.; Solomon, E. I.; Krebs, C.; Huynh, B. H.; Huang, H. W.; Moënne-Loccoz, P.; Kaderli, S.; Honecker, M.; Zuberbühler, A. D.; Marzilli, L.; Cotter, R. J.; Karlin, K. D. *Inorg. Chem.* **2007**, *46*, 3889.
(28) Chufan, E. E.; Mondal, B.; Gandhi, T.; Kim, E.; Rubie, N. D.; Moënne-Loccoz, P.; Karlin, K. D. *Inorg. Chem.* **2007**, *46*, 6382.
(29) Halime, Z.; Kieber-Emmons, M. T.; Qayyum, M. F.; Mondal, B.; Gandhi, T.; Puiu, S. C.; Chufán, E. E.; Sarjeant, A. A. N.; Hodgson, K. O.; Hedman, B.; Solomon, E. I.; Karlin, K. D. *Inorg. Chem.* **2010**, *49*, 3629.
(30) Kieber-Emmons, M. T.; Qayyum, M. F.; Li, Y.; Halime, Z.; Hodgson, K. O.; Hedman, B.; Karlin, K. D.; Solomon, E. I. *Angew. Chem., Int. Ed. Engl.* **2011**, In press (http://dx.doi.org/10.1002/anie.201104080).
(31) Lehnert, N.; Ho, R. Y.; Que, L.; Solomon, E. I. *J. Am. Chem. Soc.* **2001**, *123*, 12802.
(32) The β-spin $3d_{z^2}$ is mixed with nearby porphyrin orbitals which results in the z^2 character spread over $311-313\beta$.
(33) Yamaguchi, K.; Jensen, F.; Dorigo, A.; Houk, K. N. *Chem. Phys. Lett.* **1988**, *149*, 537.
(34) Ferguson, J.; Guggenheim, H. J.; Tanabe, Y. *J. Phys. Soc. Jpn.* **1966**, *21*, 692.
(35) The BP86 functional predicts the porphyrin orbitals at too high in energy and thus gives nonphysical TD results.
(36) Components were determined by orienting the O—O bond along the *y* axis and performing a Mulliken population analysis of the O_2^{2-} p_x and p_z contributions to 307α.
(37) Lehnert, N.; Ho, R. Y.; Que, L.; Solomon, E. I. *J. Am. Chem. Soc.* **2001**, *123*, 8271.
(38) Rich, P. R.; Rigby, S. E.; Heathcote, P. *Biochim. Biophys. Acta* **2002**, *1554*, 137.
(39) Frisch, M. J.; et al. *Gaussian03*; Gaussian, Inc.: Wallingford, CT, 2004.
(40) Kieber-Emmons, M. T. *Lumo*, Version 0.9b; Burlingame, CA, 2011.
(41) Tenderholt, A. L. *QMForge*, Version 2.1; Stanford University: Stanford, CA, 2007.
(42) Jamroz, M. H. *Veda4XL*; Drug Institute: Warsaw, Poland, 2010.